



Geochemistry, Geophysics, Geosystems

RESEARCH ARTICLE

10.1002/2017GC007120

Kev Points:

- Body-wave scattering kernels are derived for 3-D imaging for both P and S wave receiver functions
- The forward problem is approximated using ray theory resulting in a computationally efficient method
- The imaging method is demonstrated using synthetic data calculated for a hypothetical subduction zone model

Supporting Information:

- Supporting Information S1
- Data Set S1
- Data Set S2
- Data Set S3
- Movie S1
- Movie S2

Correspondence to:

S. Hansen, steven.hansen@mq.edu.au

Citation:

Hansen, S. M., & Schmandt, B. (2017). *P* and *S* wave receiver function imaging of subduction with scattering kernels. *Geochemistry, Geophysics, Geosystems,* 18, 4487–4502. https://doi.org/10.1002/2017GC007120

Received 7 JUL 2017 Accepted 26 OCT 2017 Accepted article online 3 NOV 2017 Published online 15 DEC 2017

P and S Wave Receiver Function Imaging of Subduction With Scattering Kernels

S. M. Hansen^{1,2} D and B. Schmandt¹

¹Department of Earth and Planetary Sciences, MSCO3-2040, 1 University of New Mexico, Albuquerque, NM, USA, ²Department Department of Earth and Planetary Sciences, Macquarie University, North Ryde, Sydney, NSW, Australia

Abstract A method for scattered wave imaging in 3-D with both teleseismic *P* and *S* wave receiver function data is introduced. The approach relies on body-wave scattering kernels that are derived from the adjoint data sensitivity kernels which are typically used for full waveform tomography. The forward problem is approximated using ray theory, yielding a computationally efficient imaging algorithm that can resolve dipping and discontinuous interfaces using both *P* and *S* wave receiver functions. Traveltime fields for the incident teleseismic arrivals and the receiver point-sources are obtained by solving the Eikonal equation using a Fast Marching code which can handle a 3-D reference velocity model. An energy stable finite-difference method is used to simulate elastic wave propagation in a 2-D hypothetical subduction zone model. The resulting synthetic *P* and *S* wave receiver function data sets are used to validate the imaging method. The kernel images are compared with those generated by the Generalized Radon Transform and Common Conversion Point Stacking methods. These results demonstrate the potential of the kernel imaging approach for constraining lithospheric structure in complex geologic environments with sufficiently dense recordings of teleseismic data. Potential imaging targets include short-wavelength compositional variations in the mantle wedge and the slab's lithosphere-asthenosphere boundary.

1. Introduction

Scattered wave imaging is critical for constraining the internal structure of the Earth and is the primary method used to determine the location and magnitude of seismic velocity discontinuities in the subsurface. Targeted arrays of three-component broadband seismometers are routinely deployed to constrain crust and mantle structure with passive recordings (e.g., IRIS-PASSCAL program) and scattered wave imaging is an important tool for these studies. Imaging is typically performed using steeply incident body-waves produced by earthquakes at teleseismic distances, i.e., the receiver function method (Langston, 1979; Vinnik, 1977). *P* wave receiver functions have been used to constrain several fundamental Earth structures, including the crust-mantle boundary (e.g., Gilbert, 2012) and the mantle transition zone (e.g., Lawrence & Shearer, 2006). Additionally, *S* wave receiver functions have more recently emerged as a method for constraining the lithosphere-asthenosphere boundary (Fischer et al., 2010; Rychert & Shearer, 2009) and have led to the discovery of enigmatic midlithosphere mantle discontinuities (Abt et al., 2010; Ford et al., 2010; Selway et al., 2015).

P and S wave receiver function data have different strengths and provide complementary information for structural studies. S wave data are lower frequency due to attenuation as well as lower fold and higher noise because of complications arising from the S-SKS crossover at \sim 82° epicentral distance (Yuan et al., 2006). However, S-to-p conversions arrive prior to the direct S wave arrival and are not interfered with by freesurface reverberations as is the case for the P-to-s conversions in P wave receiver functions (see Kind et al., 2012 for a review). Despite early investigations of teleseismic S wave scattering (Faber & Müller, 1980; Jordan & Frazer, 1975; Langston, 1979), the use of P wave receiver functions has dominated the field until recently. Thus, efforts to improve scattered wave imaging techniques have focused exclusively on P wave data (e.g., Rondenay, 2009). As a result, traditional 1-D common conversion point (CCP) stacking (Dueker & Sheehan, 1997) is the only conventional imaging approach currently available for S wave receiver function analysis (e.g., Lekic et al., 2011; Levander & Miller, 2012) which makes it difficult to directly compare imaging results from these two data sets (Hansen et al., 2015).

The CCP approach remains popular, even with *P* wave data, because it has several advantageous properties: it is relatively easy to implement, computationally efficient, can be used for 2-D seismic arrays (as opposed

© 2017. American Geophysical Union. All Rights Reserved.

to a 1-D linear arrays), and can be adapted approximately to account for 3-D velocity models (Levander & Miller, 2012; Schmandt et al., 2012). However, CCP images are degraded in the presence of lateral inhomogeneities such as dipping or discontinuous interfaces (Cheng et al., 2016; Morozov, 2004), both of which are not accounted for in the CCP method which is founded upon the assumption of minor deviations from a 1-D velocity structure (subhorizontal discontinuities). This is a potentially significant limitation because P wave receiver functions studies often target geologic structures that are laterally heterogeneous. Examples include the dipping megathrust interface (e.g., Abers et al., 2009; Audet et al., 2009) and the low-velocity mantle wedge (Bostock et al., 2002) in subduction zones as well as terrane boundaries and continental suture zones (e.g., Nábělek et al., 2009; Stanciu et al., 2016). S wave receiver functions have also been used for crustal imaging in orogens (e.g., Hansen & Dueker, 2009; Hopper et al., 2017) but are more routinely used to investigate the topography of the lithosphere-asthenosphere boundary (e.g., Kumar et al., 2005; Lekić & Fischer, 2014) and discontinuous interfaces within the mantle lithosphere (Hansen et al., 2015; Hopper et al., 2014). The effects of lateral heterogeneities on S wave CCP images are less well understood; however, Lekić and Fischer (2017) demonstrated several pathologies and find that source-receiver geometry is an important consideration. These studies highlight the need for methods that are capable of imaging 3-D structures with both P and S wave receiver function data.

The primary goal of this work is to connect some of the theoretical machinery from the field of full waveform inversion (FWI), specifically the adjoint data sensitivity kernels (e.g., Tromp et al., 2005) to the problem of scattered wave imaging with receiver functions. The strategy employed is similar to that of Dahlen et al. (2000) whereby ray theory is used to approximate the forward and adjoint problems rather than using full numeric wavefield simulations which results in a in a computationally efficient method. This approach results in the derivation of receiver function scattering kernels which are capable of imaging in 3-D using laterally variable velocity models for both *P* and *S* wave receiver functions. The feasibility of the proposed imaging method is demonstrated using synthetic receiver functions calculated for a hypothetical subduction zone model using an energy stable finite-difference method.

1.1. Previous Imaging Work

A notable advance in receiver function imaging was made in a series of papers (Bostock et al. 2001; Rondenay et al., 2001; Shragge et al., 2001) based upon the generalized radon transform (GRT) and its inverse (Beylkin & Burridge, 1990). The GRT method is capable of imaging in laterally heterogeneous isotropic media and has been successfully applied to several subduction zones using data collected by dense linear seismic arrays (e.g., Rondenay et al., 2008). One of the benefits of this method is that it can be used to image with scattered waves generated by the up-going direct *P* wave arrival as well as the two down-going free-surface phases PP and PS. The original GRT method has some drawbacks; however, for example, it is implemented using a 1-D reference velocity model which can lead to imaging problems in laterally heterogeneous regions. The method was also designed for linear arrays oriented approximately orthogonal to local geologic strike and so imaging is performed in 2.5-D, i.e., out of plane symmetry is assumed. The GRT method has recently been extended to 3-D imaging by Liu and Levander (2012) but only for direct P-to-s (Ps) scattering (no free-surface phases) and is computationally expensive requiring the use of a cluster. Finally, the GRT method was developed primarily to image with *P* wave receiver functions and has not been implemented to image with *S* wave data.

The CCP and GRT methods are perhaps the most widely used imaging methods for observational receiver function data but several other approaches have been developed. These include Kirchhoff migration (Bostock, 2002; Cheng et al., 2016; Levander et al., 2005; Wilson & Aster, 2005), plane wave migration (Poppeliers & Pavlis, 2003), wave equation migration (Chen et al., 2005), and elastic reverse time migration (Shang et al., 2012). Each of these approaches has different strengths and weaknesses; however, we note that none of the available methods are currently implemented for correctly imaging dipping features in 3-D with both *P* and *S* wave receiver function data.

2. Adjoint Method

A recent theoretical development in seismic imaging is *full waveform inversion* (FWI, see the review by Virieux & Operto (2009) or Fichtner (2010)) where the full-physics of wave propagation are accounted for by simulating the elastodynamic wave equation using numeric methods, such as the spectral element method

(Komatitsch & Tromp, 1999; Tromp et al., 2008). FWI can naturally account for the complexities of wave propagation in a 3-D heterogeneous material; however, solving the forward problem requires significant computational resources (e.g., Chen et al., 2007). The demands of forward modeling have led to steepest descent style approaches where the seismic velocity model and the simulated wavefield are iteratively updated to match the recorded data and minimize the objective function. In this scheme, the Fréchet derivatives of the data misfit functional (the sensitivity kernels) with respect to the current model are calculated using the adjoint method (e.g., Plessix, 2006). The next section recalls the basic equations underlying this method which are needed for the receiver function scattering kernels.

Following the derivation of Tromp et al. (2005), the misfit between the observed three-component displacement wavefield \mathbf{u} and the predicted wavefield \mathbf{u}_0 for a known reference model \mathbf{m}_0 is defined as

$$\chi(\mathbf{m}_0) = \frac{1}{2} \|\mathbf{u} - \mathbf{u}_0\|_{L^2}^2, \tag{1}$$

where the L^2 norm is defined

$$\|\mathbf{v}\|_{L^2}^2 = \int_{\Omega} \int_{0}^{T} \mathbf{v} \cdot \mathbf{v} dt d\mathbf{x}.$$
 (2)

In equation (2), $\mathbf{x} \in \Omega, t \in (0,T)$ is the domain of the vector-valued function $\mathbf{v}(\mathbf{x},t)$ and \cdot denotes contraction. The perturbation of the misfit with respect to the model variation $\delta \mathbf{m}$ can be written as the volume integration

$$\delta_{\mathbf{m}}\chi(\mathbf{m}_{0}) = \int_{V} \frac{\delta\rho}{\rho_{0}} K_{\rho}(\mathbf{x}) + \frac{\delta\lambda}{\lambda_{0}} K_{\lambda}(\mathbf{x}) + \frac{\delta\mu}{\mu_{0}} K_{\mu}(\mathbf{x}) d^{3}\mathbf{x}, \tag{3}$$

where $K_{\lambda,\mu,\rho}(\mathbf{x})$ are the sensitivity kernels for an isotropic elastic material and are given by

$$K_{\rho}(\mathbf{x}) = -\int_{0}^{T} \rho_{0}(\mathbf{x}) \mathbf{u}^{\dagger}(\mathbf{x}, T - t) \cdot \partial_{t}^{2} \mathbf{u}_{0}(\mathbf{x}, t) dt$$

$$K_{\lambda}(\mathbf{x}) = -\int_{0}^{T} \lambda_{0}(\mathbf{x}) [\nabla \cdot \mathbf{u}_{0}(\mathbf{x}, t)] \left[\nabla \cdot \mathbf{u}^{\dagger}(\mathbf{x}, T - t)\right] dt , \qquad (4)$$

$$K_{\mu}(\mathbf{x}) = -\int_{0}^{T} 2\mu_{0}(\mathbf{x}) \varepsilon_{0}(\mathbf{x}, t) : \varepsilon^{\dagger}(\mathbf{x}, T - t) dt$$

where \mathbf{u}^{\dagger} is the *adjoint wavefield* and ε is the strain field defined by the displacement \mathbf{u} . The adjoint wavefield results from back-propagating the wavefield difference $\Delta \mathbf{u} = \mathbf{u} - \mathbf{u}_0$ from point sources at the receiver locations (Tarantola, 1984; Tromp et al., 2005). Rather than using the Lamé parameters λ and μ , the kernels may also be expressed in terms of P and S wave seismic velocities α and β by

$$K_{\alpha} = 2 \frac{\lambda + 2\mu}{\lambda} K_{\lambda}
K_{\beta} = 2K_{\mu} - 4 \frac{\mu}{\lambda} K_{\lambda} ,
K_{\rho'} = K_{\lambda} + K_{\mu} + K_{\rho}$$
(5)

where $K_{\rho'}$ is the residual density kernel (Tromp et al., 2005).

2.1. Relationship to Migration

The adjoint method provides a general framework for the seismic parameter estimation problem and is typically used to estimate an absolute velocity model from the recorded data. For example, FWI of short-period teleseismic body-waves is an active research topic and has shown promising results in both 2.5-D (e.g., Baker & Roecker, 2014) and 3-D (Monteiller et al., 2015; Wang et al., 2016). The objective of scattered wave imaging (migration) is different, and aims to resolve the short-wavelength velocity perturbations that are

responsible for generating the observed scattered arrivals; however, the problems are clearly related (Zhu et al., 2009). The primary goal of migration is to produce images for structural interpretation, e.g., determining crustal thickness, rather than to constrain absolute seismic velocity (although this can be done as well). In the receiver function migration framework considered here, a smooth background velocity model is assumed and the reference wavefield \mathbf{u}_0 consists solely of the direct arrival and the two free-surface phases. The wavefield difference $\Delta \mathbf{u}(t, \mathbf{x}_r)$ thus represents the full three-component receiver function for the seismometer located at \mathbf{x}_r with the direct arrival \mathbf{u}_0 removed (Rondenay, 2009).

The waveform difference used to define the misfit functional in equation (1) is known to be a poor parameterization for the FWI problem because it results in strong nonlinearity (Gauthier et al., 1986) and several alternatives are available (e.g., Gee & Jordan, 1992). However, this is a reasonable choice for the imaging problem and the resulting sensitivity kernels in equation (4) represent the reverse time migration (RTM) approach used in active-source seismology (Tarantola, 1984). For example, the K_{λ} kernel is proportional to the zero-lag cross-correlation between the source and time-reversed receiver pressure wavefields and is one of the "imaging conditions" used for seismic reflection processing in an acoustic medium (Claerbout, 1971). From the perspective of elastic RTM (Chang & McMechan, 1987), the K_{μ} kernel provides an imaging condition for shear-waves and mixed mode scattering, although other choices are possible (e.g., Yan & Sava, 2008).

3. Scattering Kernels

One of the primary limitations of the FWI and RTM methods for imaging in 3-D with receiver function data is the significant computational expense of the large-scale forward problem. A complete wavefield modeling volume that contains both the teleseismic sources and the receiver locations would require a global-scale model with temporal sampling up to \sim 1 Hz which is impractical with current modeling approaches. Hybrid methods have been proposed where regional (100s of km in scale) wave propagation in a locally heterogeneous model is simulated on the receiver side of the earth and the incoming teleseismic wavefield is modeled using a simplified earth model (e.g., Monteiller et al., 2013; Tong et al., 2014). This strategy is more efficient but still requires the use of high performance computing resources.

Instead of using numeric wavefield simulations to calculate \mathbf{u}_0 and \mathbf{u}^\dagger , the forward problem is approximated using ray theory to calculate the sensitivity kernels (Dahlen et al., 2000). For the case of receiver function imaging and a smooth reference velocity model, it is assumed that for each earthquake the incident wavefield consists of a single phase with a known source time function. Assuming that no reflections or caustics are encountered within the image volume, the ray theoretical reference wavefield is

$$\mathbf{u}_0(\mathbf{x},t) = \hat{\mathbf{p}}A_{xs}s(t-\tau_{xs}),\tag{6}$$

where $\tau_{xs} = \tau(\mathbf{x}, \mathbf{x}_s)$ is the traveltime field from the source location \mathbf{x}_s to the image point \mathbf{x} (solves Eikonal) and $\hat{\mathbf{p}}$ is the unit length polarization vector at \mathbf{x} . The source time function s(t) is assumed to be constant in space but is the effective source following receiver function source normalization (deconvolution). The amplitude term in (6) is

$$A_{xs} = (\rho c)^{-1/2} (c_s \Re_{xs})^{-1}, \tag{7}$$

where $c=c(\mathbf{x})$ is the velocity of the incident wave (either *P* or *S* wave velocity) and $c_s\Re_{xs}=c\Re_{sx}$ is the *relative* geometric spreading term (obeys reciprocity) from the source to the image point. The two down-going free-surface phases associated with the direct arrival have the same form as (6) but with different polarities and traveltime functions.

The adjoint wavefield is approximated using the ray theoretical Green's function (Cerveny, 2005) for a point source in the reference velocity model which results in the form

$$\mathbf{u}^{\dagger}(\mathbf{x},t) = -\frac{1}{4\pi} \sum_{r} \sum_{rays} \hat{\mathbf{p}}' A_{xr} \hat{\mathbf{p}}_{r} \cdot \Delta \mathbf{u}(\mathbf{x}_{r}, T - t + \tau_{xr}), \tag{8}$$

where the first summation is over all receiver locations \mathbf{x}_r and the second summation is over all rays from the receiver to the scattering point \mathbf{x} , $\hat{\mathbf{p}}_r$, and $\hat{\mathbf{p}}'$ are the polarization vectors of the rays at these locations and τ_{xr} are the traveltime functions. The amplitude term in (8) is given by

$$A_{xr} = (\rho' c' \rho_r c_r)^{-1/2} (c_r \Re_{xr})^{-1}, \tag{9}$$

where c' and c_r are the ray velocities, $c_r \Re_{xr} = c' \Re_{rx}$ is the geometric spreading term. Note that it has again been assumed that the material is smoothly varying, i.e., no reflection/transmission of the rays occurs, and that no caustics are encountered, otherwise additional terms are needed in (8).

Combining the ray theoretical reference and adjoint wavefields in (6) and (8) with the sensitivity kernels in (4) yields the final scattering kernels

$$K_{\rho}^{ray}(\mathbf{x}) = \frac{1}{4\pi} \sum_{r} \sum_{rays} A_{xr} A_{xs} \left[\hat{\mathbf{p}}' \cdot \mathbf{S}_{\rho} \cdot \hat{\mathbf{p}} \right] \left[\hat{\mathbf{p}}_{r} \cdot \mathbf{c}_{rs} \right]$$

$$K_{\lambda}^{ray}(\mathbf{x}) = \frac{1}{4\pi} \sum_{r} \sum_{rays} A_{xr} A_{xs} \left[\hat{\mathbf{p}}' \cdot \mathbf{S}_{\lambda} \cdot \hat{\mathbf{p}} \right] \left[\hat{\mathbf{p}}_{r} \cdot \mathbf{c}_{rs} \right],$$

$$K_{\mu}^{ray}(\mathbf{x}) = \frac{1}{4\pi} \sum_{r} \sum_{rays} A_{xr} A_{xs} \left[\hat{\mathbf{p}}' \cdot \mathbf{S}_{\mu} \cdot \hat{\mathbf{p}} \right] \left[\hat{\mathbf{p}}_{r} \cdot \mathbf{c}_{rs} \right]$$

$$(10)$$

where $\mathbf{S}_{\lambda,\mu,\rho}$ are the *scattering tensors* (Dahlen et al., 2000) and are defined as

$$\begin{aligned} \mathbf{S}_{\rho} &= \rho_0(\mathbf{x}) \mathbf{I} \\ \mathbf{S}_{\lambda} &= \lambda_0(\mathbf{x}) \frac{1}{cc'} \left(\hat{\mathbf{k}}' \hat{\mathbf{k}} \right) \\ \mathbf{S}_{\mu} &= \mu_0(\mathbf{x}) \frac{1}{cc'} \left[\left(\hat{\mathbf{k}}' \cdot \hat{\mathbf{k}} \right) \mathbf{I} + \hat{\mathbf{k}} \hat{\mathbf{k}}' \right] \end{aligned}$$
(11)

where $\hat{\mathbf{k}}$ and $\hat{\mathbf{k}}'$ are the unit length wave vectors for the source and receiver rays at the scattering point \mathbf{x} . The term \mathbf{c}_{rs} is the cross-correlation between wavefield difference (receiver function) and the second derivative of the source time function

$$\mathbf{c}_{rs} = \int \Delta \mathbf{u}(\mathbf{x}_r, t + \tau_{rs}) \partial_t^2 s(t) dt$$
 (12)

at a lag time corresponding to the net source-to-scatterer-to-receiver traveltime $\tau_{rs} = \tau_{rx} + \tau_{xs}$.

Each scattering kernel has three main components, the first $A_{xr}A_{xs}$ is an amplitude term which includes the net effect of geometric spreading from source-to-scatterer-to-receiver. The second term is $\hat{\mathbf{p}}' \cdot \mathbf{S} \cdot \hat{\mathbf{p}}$ and defines the radiation pattern for a point scatterer at \mathbf{x} due to an incident ray with polarization $\hat{\mathbf{p}}'$ resulting in a scattered ray with polarization $\hat{\mathbf{p}}'$ (Dahlen et al., 2000). The final term $\hat{\mathbf{p}}_r \cdot \mathbf{c}_{rs}$ is the projection of the lagged three-component cross-correlation trace onto the polarization vector of the scattered ray at the receiver

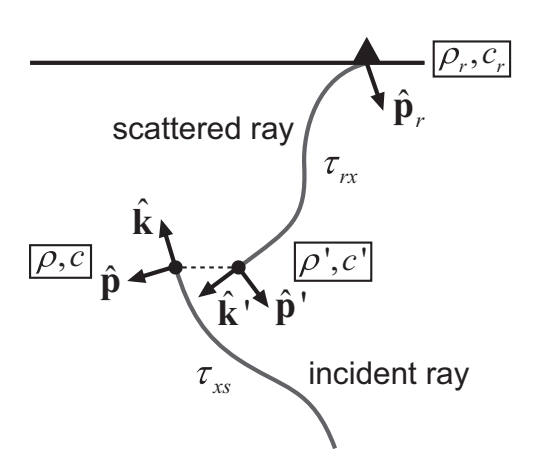


Figure 1. Ray diagram showing the spatial distribution of terms used in the scattering kernel definitions in equations (10) and (11). The incident and scattered rays are offset horizontally (dashed line) at the scattering point (black circle) for clarity and the receiver location is denoted by a black triangle. In this example, both the incident and scattered phases are *S* waves.

location. Figure 1 shows the spatial distribution of the terms in (10) and (11). Note that the direction of the scattered ray is from the receiver to the scattering point.

3.1. Kernel Examples

Three examples of scattering kernels relevant to receiver function imaging are shown in Figure 2 for a single receiver (triangle) and a uniform velocity model. The incident wavefield is an up-going plane wave and the kernels are shown for the scattered arrival corresponding to a horizontal discontinuity at 40 km depth. The kernels are overlain with the ray paths used in the CCP stacking approach which assumes that scattered arrivals are generated from a horizontal interface (CCP image point in Figure 2) (Dueker & Sheehan, 1997). In contrast to the CCP method, the scattering kernels can account for arrivals that are generated anywhere along a surface in the image volume defined by the phase travel time (scattering isochron) and are therefore capable of imaging dipping features as will be demonstrated.

Two novel observations arise from this analysis. The first is that the direct S-to-p (Sp) scattering kernel relevant to S wave receiver function

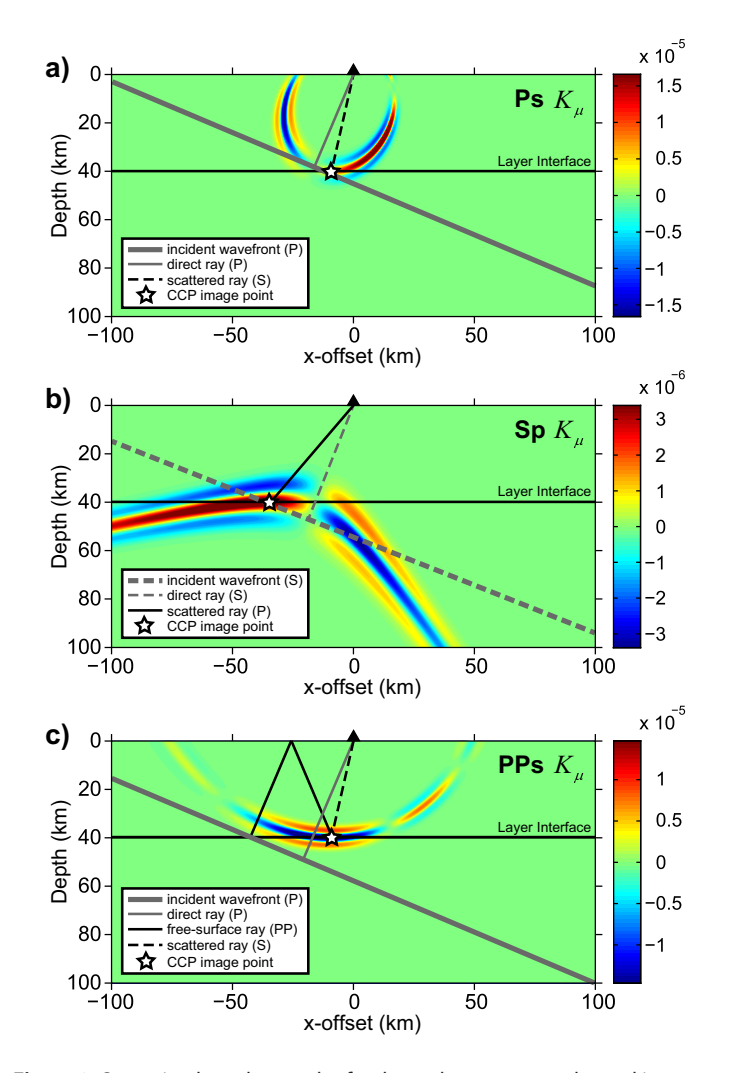


Figure 2. Scattering kernel examples for three phases commonly used in receiver function imaging. (a) Direct P-to-s (Ps) forward scattering, (b) direct S-to-p (Sp) forward scattering, and (c) free-surface reflected PP-to-s (PPs) backward scattering. Kernels are calculated using a homogeneous velocity model and the scattered phase timing and polarity are determined for a horizontal interface occurring at 40 km depth. The polarity of the kernels denotes the sign of the velocity perturbation required to match the observed scattered phase. Each plot also contains the ray paths and scattering point assumed by the 1-D CCP stacking method.

imaging is significantly different than that of the direct P-to-s (Ps) kernel. This is because the scattering isochrons have different curvature due to the relative velocity of the scattered phase compared to the direct arrival. Second, the Sp and the free-surface reflected PP-to-p (PPp) scattered phases are better suited for imaging a horizontal interface given the geometry of their sensitivity kernels. In contrast, the Ps kernel has relatively high curvature and the kernel amplitude diminishes near a horizontal interface. These differences in kernel geometry also suggest that Ps imaging requires a higher station density than that of Sp or the free-surface multiple phases.

3.2. Fast Marching Implementation

The scattering kernels for uniform or 1-D velocity models can be determined straightforwardly using analytic ray solutions (e.g., Figure 2). However, these kernels may result in inaccurate images due to lateral variations in earth structure which are often encountered in practice. To overcome this limitation, the traveltime fields for a heterogeneous reference velocity model are obtained by solving the Eikonal equation using the Fast Marching Method (FMM) software from Rawlinson and Sambridge (2004). The scattering kernels for each source-receiver pair require a total of five traveltime solutions to compute all first-order scattering interactions. Three are needed for the teleseismic source, including the incoming phase and the two downgoing free-surface phases, and two are needed for the receiver point source, the direct P wave and direct S wave arrivals. The arrival times for each teleseismic source are calculated only within the model domain. The arrival times of the incoming phase along the boundary are determined by the 1-D reference earth model ak135 (Kennett et al., 1995).

In addition to the travel times, the kernels require the geometric spreading and polarization vectors, which can be calculated for a heterogeneous model using dynamical ray tracing (Cerveny, 2005). The purpose of migration is primarily kinematic, i.e., to correctly image the location of the scatterer, and so for efficiency we make a series of approximations to avoid dynamical ray tracing. The incident wavefield is nearly a plane wave for teleseismic sources and so the spreading term \Re_{xs} is assumed to be constant over the image volume. The point source geometric spreading \Re_{xr} factor is approximated as $\|\mathbf{x}-\mathbf{x}_r\|$ which is only correct for a homogeneous model. Strategies exist for calculating the geometric spreading directly from the traveltime fields

(e.g., Vidale & Houston, 1990) but are not implemented here. The wave vectors and *P* wave polarizations are obtained from the (normalized) gradient of the traveltime fields. The *S* wave polarizations are in the traveltime tangent plane and are calculated via rotation of the wave vector. The definition of the two degenerate *S* wave polarizations (isotropic), e.g., SV and SH, is somewhat arbitrary at the scattering point but must be consistent with the polarizations as defined at the receiver location (Figure 1). These simplifications allow the full scattering kernels to be approximated directly from the traveltime fields and ray tracing results of the FMM code. The approximations employed do not prevent accurate imaging of complex lithospheric interfaces within laterally heterogeneous background velocity structures as shown next.

4. Wavefield Simulation

4.1. Finite-Difference Method

The proposed imaging method is tested on synthetic receiver function data sets generated using a 2-D finite-difference algorithm that solves the elastic wave equation in time-displacement form (Duru et al.,

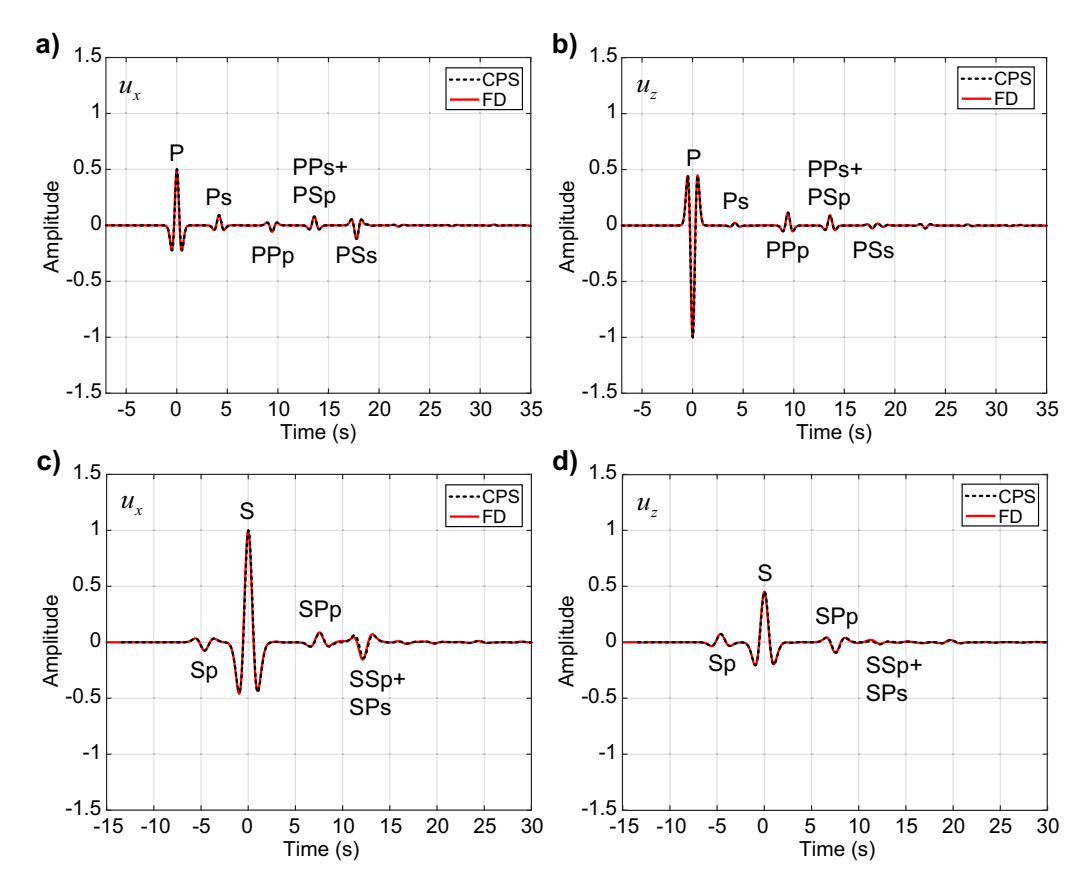


Figure 3. Comparison between the receiver functions calculated by finite-difference simulation and synthetic traces produced by the CPS package (Herrmann, 2013). A 1-D velocity model is used for both calculations and is composed of a single 35 km thick layer overlying a uniform half-space. The vertical and horizontal components of displacement are plotted in (a) and (b) for an incident *P* wave are with a horizontal slowness of 0.06 s/km and a Ricker source-time function with a center frequency of 0.8 Hz. Results for an *S* wave source are shown in (c) and (d) with a horizontal slowness of 0.1 s/km and a 0.4 Hz source function. All first-order scattering modes of the direct and free-surface phases are labeled.

2014). This energy stable numeric method relies on the variable coefficient summation-by-parts derivative stencils (Mattsson, 2012) and weak boundary condition enforcement using simultaneous approximation terms (see Svärd & Nordström (2014) for a review). The approach of Duru et al. (2014) is implemented using fourth-order accurate time-stepping and fourth-order accurate spatial derivative stencils. Absorbing boundary conditions (Petersson & Sjögreen, 2009) are applied on the sides and bottom of the model and the zero-traction free-surface condition is used along the top boundary. A rigorous error analysis of this approach can be found in Duru et al. (2014). However, our implementation was applied to a layer over a half-space velocity model and the resulting traces compare favorably with the 1-D synthetic receiver functions calculated using the CPS code package (Herrmann, 2013) (Figure 3).

The source time function used in all simulations is a Ricker wavelet (second derivative of a Gaussian) using a center frequency of 0.8 Hz for *P* wave sources and 0.4 Hz for *S* wave sources. The motivation for a Ricker source function (besides its analytic properties) is provided by the kernel correlation term (12) which involves the second derivative of the source function. To avoid numerical dispersion, the model is spatially sampled at 18 points per minimum wavelength at the center frequency, resulting in a sampling of 262 and 525 m for *P* and *S* wave sources, respectively. The time increment used is

$$\Delta t = 0.5 \frac{\Delta x}{\max \sqrt{\alpha^2 + \beta^2}},\tag{13}$$

where α and β are the *P* and *S* wave velocities and $\Delta x = \Delta z$ is the spatial sampling. The 0.5 scaling in (13) was determined empirically and was found to maintain stability in simulations with absorbing boundary conditions. This choice results in a time step of 14.2 and 28.3 ms for the *P* and *S* wave sources.

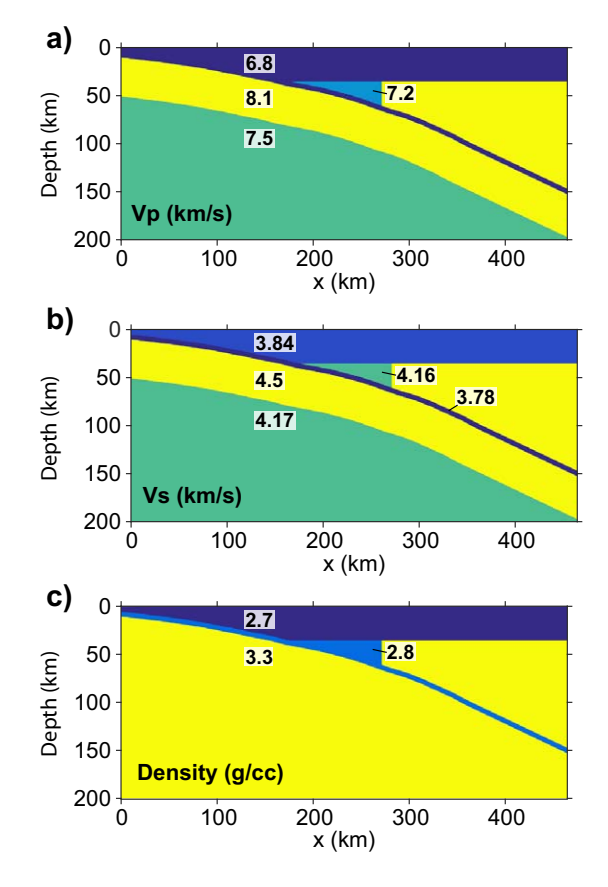


Figure 4. The elastic properties of the hypothetical subduction zone model. The slab consists of a 5 km thick oceanic crust, a 40 km thick mantle lithosphere, and an underlying lower-velocity asthenosphere. The upper-plate contains single crust and mantle layers. A slower mantle wedge region is included that terminates laterally at a slab decoupling depth of 60 km. The velocity and density values of each model region are labeled. The slab depth profile is taken from the model of McCrory et al. (2012) for the Cascade Subduction Zone near 46° latitude.

4.2. Subduction Zone Model

Synthetic data are calculated for a hypothetical 2-D subduction zone model consisting of three components: a dipping three-layer slab with crust-mantle and lithosphere-asthenosphere velocity discontinuities, a horizontal two layer upper-plate with a crust-mantle boundary, and a low-velocity mantle wedge region (Figure 4). Simulations are performed for a suite of incoming plane waves which are introduced into the simulation using "injection" along the bottom of the model (absorbing boundary conditions are applied after its passage). Ten P wave sources are simulated with horizontal slowness ranging ± 0.04 – 0.08 s/km which is representative of the direct teleseismic P wave arrivals used in receiver function studies. Six direct S wave (± 0.09 – 0.11 s/km) events are also simulated to produce an S wave receiver function data set. Example wavefield snapshots of both P and S wave source simulations are shown in Figure 5. Wavefield animations for these examples are in the supporting information.

To produce the receiver function data sets, the simulated wavefields recorded at the free-surface are decimated to ~ 1 km receiver spacing, time-aligned with the direct arrival using cross-correlation and amplitude normalized. The direct arrival is removed from the data by applying a trace mute defined by the width of the source-time function. The synthetic receiver function data sets are included in the supporting information. Despite the 2-D nature of the modeling effort, it should be noted that the simulation results are valid in 3-D for the special case of out-of-plane symmetry (2.5-D) of both the velocity model and the incident wavefield (in-plane source).

5. Imaging Results

The synthetic receiver function data sets derived from the subduction zone model are used to construct scattered wave images using the ray kernels from equation (10). The traveltime fields are calculated with the FMM code using smoothed versions of the velocity models in Figure 4. The resulting kernels are linearly stacked over all source-

receiver pairs to produce images for the direct phase and the two free-surface multiples. The proposed scheme results in a relatively rapid imaging algorithm. For example, the synthetic *P* wave data set consists of 4,430 three-component receiver functions and uses a 2-D image volume sized 465 by 250 km sampled at 1 km increments. The image calculation requires about 200 s of computation time on a single CPU Linux machine using Matlab (8 core AMD processor, 32 GB RAM). The primary computational effort in this approach is calculating the traveltime fields with the 3-D FMM code for 443 stations, which takes about 2 h, but only needs to be performed once and stored for later use. For reference, the GRT code with the same model dimensions and assumption of a 1-D background velocity structure runs for about 80 min.

Scattering from a single seismic discontinuity, e.g., the Moho, should normally produce images with two bands of energy with alternating sign on either side of the interface. While this is technically correct in terms of the volumetric velocity model perturbation that is required to produce a discontinuity in a smooth background model (e.g., Burdick et al., 2013), it is less intuitive for the purposes of structural interpretation of interfaces, which are represented by zero crossings rather than local maxima. For this reason, an ad hoc 45° phase shift has been applied to the receiver function traces prior to imaging resulting in images with a single pulse (plus minor side lobes) whose maximum occurs near the interface location (see the supporting information). Additionally, the time to depth mapping differs between that of the direct arrival and the two free-surface phases which results in images with different wavelengths. Due to the increased time compression associated with scattered arrivals associated with the free-surface phases, the *P* wave receiver functions are filtered to a lower center-frequency (0.2 Hz) for the multiple images.

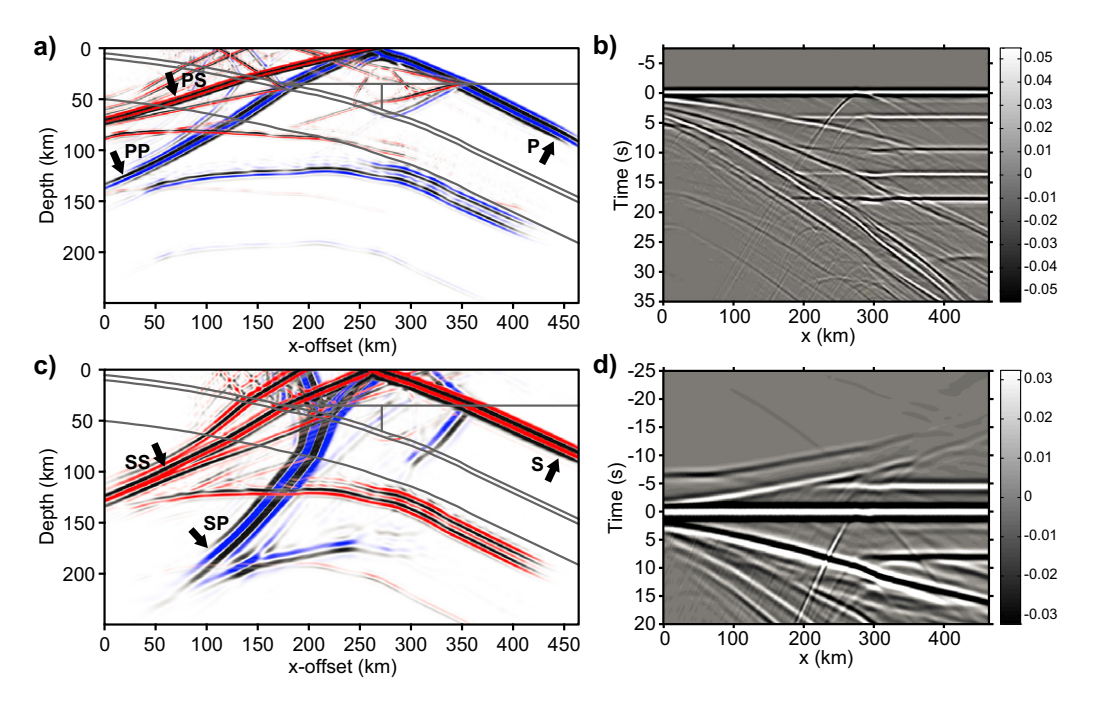


Figure 5. Finite-difference wavefield simulations for the subduction zone model. The P wave source shown in (a) and (b) is an incident plane wave with an initial slowness of +0.06 s/km. The S wave source in (c) and (d) has a slowness of +0.1 s/km. Velocity discontinuities in the subduction zone model (Figure 4) are plotted as gray lines in the wavefield snapshots Figures 5a and 5c. The direct arrival and the two free-surface reverberation phases are also labeled. The propagation directions of these phases are denoted by arrows. To facilitate wavefield visualization in these images, P and S wave modes are separated and plotted independently by calculating the divergence and curl of the displacement field. P waves are plotted in a blue-to-black color scale and S waves are red-to-black. The resulting receiver function traces are plotted in Figures 5b and 5d. The traces have been time-aligned by the direct arrival.

5.1. *P* Wave Receiver Function Images

Kernel and GRT images for direct wave scattering derived from the *P* wave receiver function data set are presented in Figures 6a and 6b. The horizontal blue band at 35 km depth on the right side of the images represents the upper-plate Moho and is well resolved. The top and bottom of the thin crustal layer of the subducting slab is imaged as two closely spaced bands of energy. Both the kernel and GRT images are affected by incorrectly migrated phases. For example, the steeply right dipping features observed beneath the slab LAB (0–200 km offset) result from the free-surface phases back-scattering off the dipping slab. The GRT image appears to be more susceptible to these artifacts than the kernel image. Additionally, the mantle wedge forms a vertically oriented velocity discontinuity that causes scattering of the direct wave. These scattered arrivals can be identified in Figures 5a and 5b as the curved wavefronts immediately trailing the direct *P* wave arrival near 275 km *x*-offset. The kernel image resolves this vertical boundary but it is not observed in the GRT image. Finally, the GRT code is limited to a 1-D background velocity model which

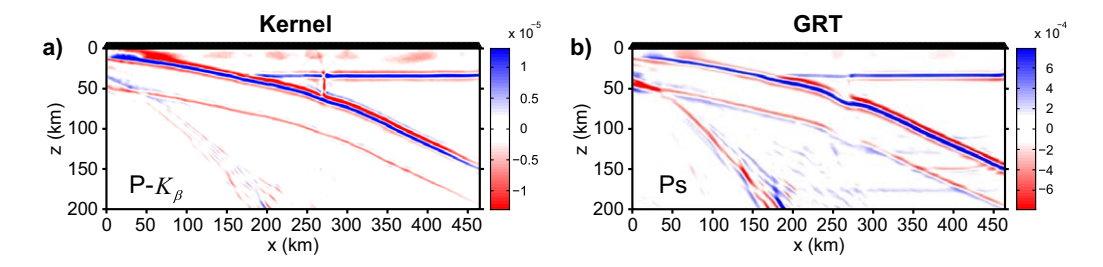


Figure 6. Comparison of kernel and GRT images for the P wave receiver function data set calculated for the subduction zone model. (a) The scattered wave image resulting from averaging all of the individual K_{β} receiver function kernels for the direct P phase. The kernels are calculated using a smoothed version of the 2-D velocity models in Figure 4. (b) The GRT image for the Ps phase using a 1-D velocity model.

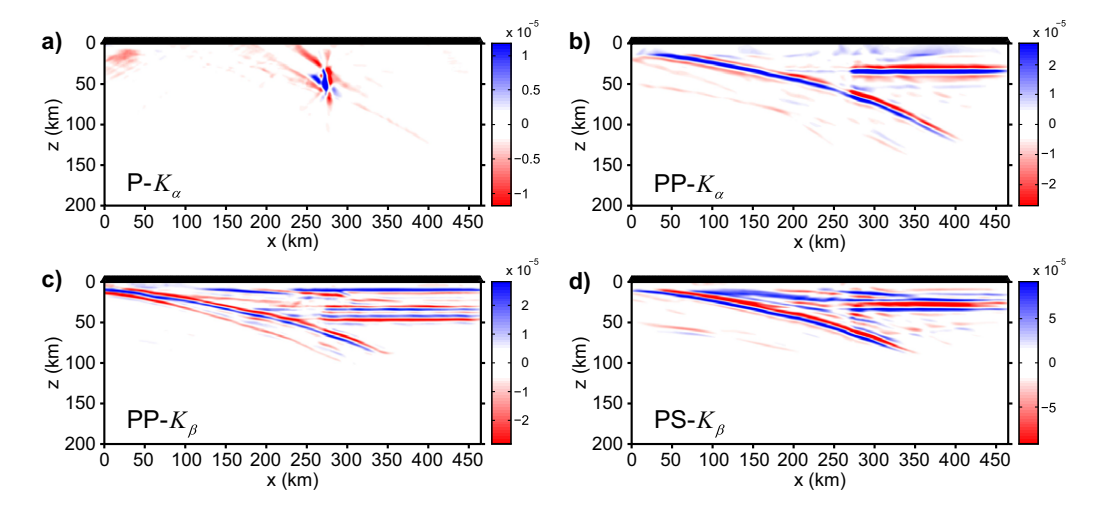


Figure 7. Additional kernel images for the P wave receiver function data set. The direct P to P scattering image is shown in (a). The receiver functions are filtered to a lower corner frequency of 0.4 Hz prior to constructing the free-surface images in (b)–(d). The free-surface PS P wave velocity kernel image is zero and is not shown.

results in image inaccuracies, primarily due to the presence of the slow mantle wedge in the subduction model (Figure 4). The surface of the slab is clearly depressed in Figure 6b beneath the wedge location and this "push-down" effect is also observed for the deeper slab LAB.

All additional kernel images for the P wave data set are contained in Figure 7. The K_{α} image for the direct P wave arrival (Figure 7a) is dominated by the edge of the wedge which is the only model feature that produces significant Pp scattering. In contrast, the PPp image (Figure 7b) resolves the boundaries of the dipping slab and upper-plate well but not the wedge. The K_{β} kernel images for the PP and PS free-surface phases (Figure 7c and 7d) resolve the surface of the slab but these images are more heavily affected by migration noise and are more difficult to interpret.

5.2. S Wave Receiver Function Images

The kernel and CCP images for the S wave receiver function data set are presented in Figure 8. The Moho of the upper-plate and the top of the subducting slab left of the mantle wedge are well imaged using the kernel method (Figure 8a). However, the deeper portion of the slab surface and the slab LAB are poorly recovered. There are several causes for this observation, one of which is the source geometry. The relatively high incidence angles of the direct S wave phases $(24^{\circ}-30^{\circ})$ with respect to vertical) means that the sources traveling up and to the right impinge upon the steeper portion of the slab at near-normal incidence, resulting in low S-to-p conversion coefficients. Similarly, the left-going sources are highly oblique to the dipping slab resulting in little scattered energy. The slab LAB is also difficult to image because it has a lower velocity contrast (7.7% Vs reduction) compared to the other discontinuities in the subduction model (Figure 4). Finally, the steeply dipping limb of the Sp scattering kernel (e.g., Figure 2b) resulting from the shallower and higher amplitude Sp conversions at the slab surface interfere with the image in the LAB region.

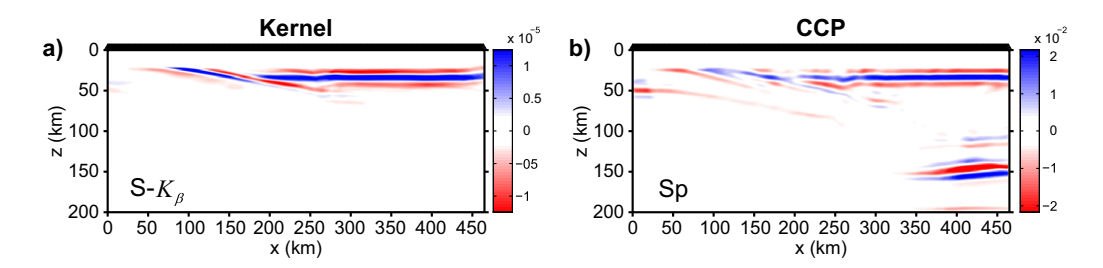


Figure 8. Comparison of kernel and CCP images for the synthetic *S* wave receiver function data set. (a) The image of all K_{β} kernels averaged all source-receiver pairs for the direct *S* phase. (b) The CCP image for the *Sp* phase.

The CCP image (Figure 8b) has a higher amplitude LAB but it is imaged at the wrong depth because the 1-D imaging assumption is particularly problematic for Sp conversions which arrive at shallow incidence angles. The CCP image is also degraded by a spurious high amplitude feature at 150 km depth on the right side of the image that is not observed in the kernel image. This feature is caused by scattering that occurs outside of the imaging domain for the left-going S wave sources and is a product of the finite-difference implementation. A 1-D velocity profile is used outside of the image domain and the lateral transition to the steeply dipping slab causes a diffracted arrival that is not properly migrated by the CCP method.

5.3. Effects of Sampling and Noise

The synthetic receiver function data sets are optimistic compared to observational data due to the lack of noise as well as the uniform and relatively dense 1 km receiver spacing. However, the impacts of increased station spacing and additive noise are explored in Figures 9 and 10. Noise traces are calculated by convolving white Gaussian noise with a Ricker wavelet so that the noise has a spectrum similar to that of the synthetic receiver functions. The magnitude of the noise variance (relative to the direct arrival) was estimated from a compilation of observed P and S wave receiver function traces used in a previous study with \sim 2,000 broadband stations (Hansen et al., 2015). Interestingly, the median variance of the S wave receiver function data set was found to be about 3.5 times larger than that of the P wave data set. The P images (Figure 9) are more sensitive to the station spacing than the S images (Figure 10) due to the higher curvature of the P skernels (Figure 2); however, the P images are higher resolution and produce the best images overall. These results suggest that the kernel imaging method will be effective for lithospheric imaging with P wave

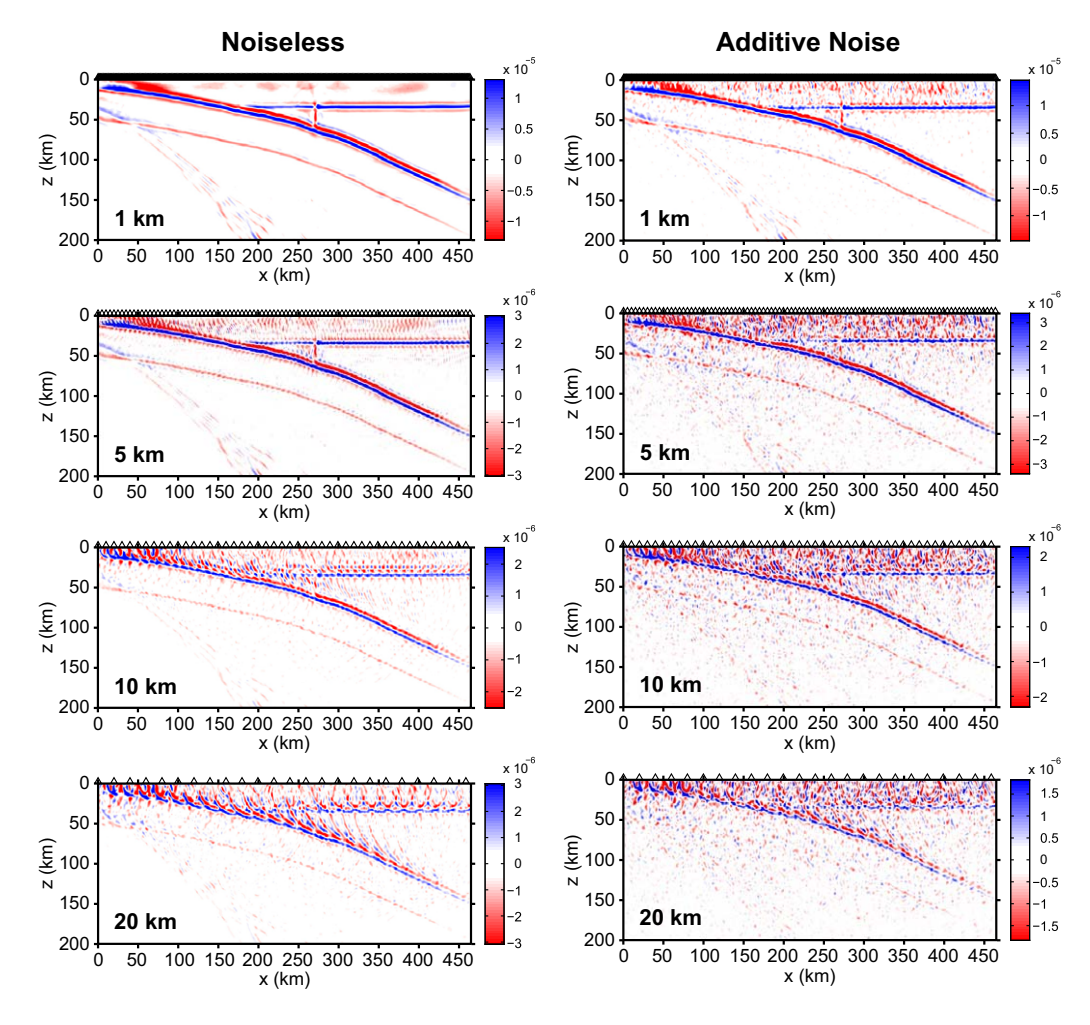


Figure 9. The effect of variable receiver spacing and additive noise on the direct P wave scattering kernel image. Receiver spacing increases from 1 km at the top (same as in Figure 6) to 20 km at the bottom. Images in the left column are noise-free and images on the right have colored noise with a variance of 8×10^{-4} .

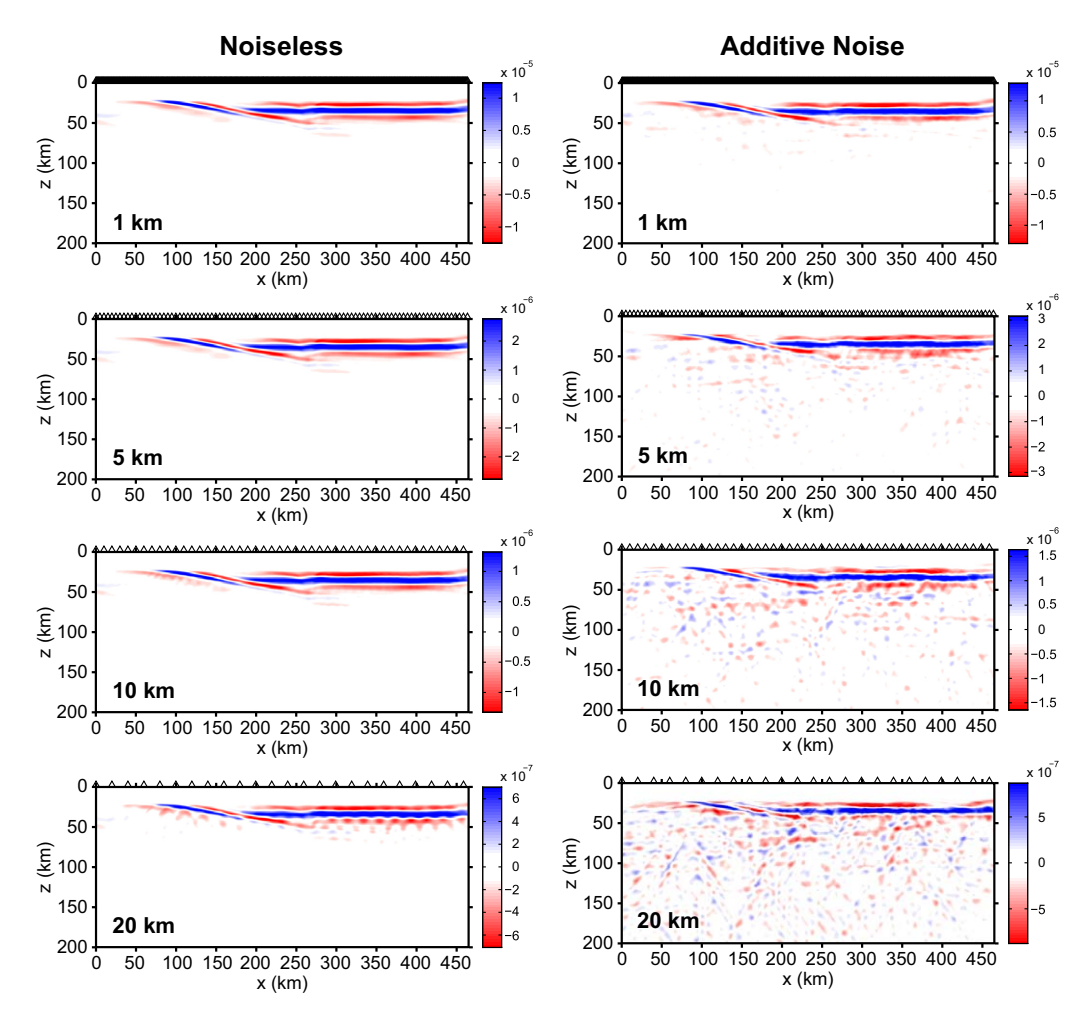


Figure 10. The same format as Figure 9 but for the *S* wave receiver function data set. The noise variance for the images in the right column is 2.8×10^{-3} .

receiver functions for arrays with a station spacing of less than about 10 km, consistent with previous numeric studies (Baker & Roecker, 2014; Tong et al., 2014). Sp scattering and free-surface phases are better suited to imaging with spatially undersampled arrays and provide complementary imaging information.

6. Discussion

The ray-theory-based kernel images (Figures 6–8) reproduce the structure of the subduction model with fidelity and demonstrate the capacity of this method to constrain subsurface structures using both *P* and *S* wave receiver function data. This approach helps to bridge a gap between traditional receiver function imaging methods such as CCP stacking and more modern approaches such as elastic reverse-time migration (RTM) (e.g., Shang et al., 2012) and full waveform inversion (FWI) (Monteiller et al., 2015). The method developed here provides an efficient framework for elastic scattered wave imaging in 3-D for both *P* and *S* wave receiver function data and thus fills a gap in existing imaging methods. A primary benefit of the proposed scattering kernels is computational efficiency. In principle, the finite-difference implementation could have been used to simulate the reference and adjoint wavefields instead of using ray theory, which is essentially the RTM approach (e.g., Shang et al., 2012). However, this would have increased the computational burden of the imaging algorithm by at least an order-of-magnitude for the 2-D example investigated here. The imaging results show that the proposed method is a promising tool for 3-D imaging with moderate computational resources for regional-scale passive-source deployments.

Teleseismic scattered wave imaging approaches are often applied at frequencies \leq 0.5 Hz, but teleseismic P waves provide high signal-to-noise ratios at higher frequencies, often up to \sim 3 Hz, which will become increasingly important as the recording density of seismic arrays continues to increase (e.g., Schmandt & Clayton, 2013). Challenges to exploiting higher frequencies in scattered wave imaging with passive data include computational efficiency and the need to accurately account for smooth 3-D velocity structure to achieve coherent stacking of scattered energy. Increasing the frequency content beyond the 0.8 Hz source used in the subduction zone demonstration of Ps imaging further widens the gap in computational burden between full elastic wavefield approaches, such as RTM, and the ray-based kernel imaging approach. Incorporating the FMM code into the kernel calculations allows the imaging method to account for smooth 3-D background velocity structure and may enable detection of finer-scale interfaces whose scattered arrivals would be migrated to inaccurate depths or degraded by incoherent stacking under the assumption of a 1-D background velocity model (e.g., Figure 6). Thus, the method is well suited to explore the full bandwidth provided by teleseismic body waves.

6.1. Possible Extensions

The methods explored in this work provide a promising technique for receiver function imaging; however, several issues remain unresolved and require additional exploration. The finite-difference method used here (Duru et al., 2014) has yet to be extended to 3-D and so only 2-D synthetics have been tested. With that said, the scattering kernel derivation and the FMM implementation are inherently 3-D and the images presented here are constructed using 2-D slices through fully 3-D kernels. The kernels back-project scattered wave energy along the entire scattering isochron and so it is possible for a large amplitude arrival to interfere with more subtle features in the image, e.g., the missing slab LAB in the *S* wave kernel image (Figure 8a). Finally, the efficacy of the proposed method has yet to be demonstrated on observational receiver function data and this will be the focus of future efforts. The focus of this work is on lithospheric imaging with receiver functions but this method could also be used for transition zone imaging and other large-scale body-wave scattering problems, such as SS precursors (e.g., Shearer, 1991). The FMM code used to calculate the traveltime fields (Rawlinson & Sambridge, 2004) accounts for a spherical earth geometry as well as the curvature of the incoming teleseismic phase (nonplanar source) and can therefore be used for these types of imaging problems.

Similar to the GRT method, the ray kernels provide intuition regarding the imaging problem because the contributions from different scattering modes and free-surface phases are separated explicitly in the imaging formulation (e.g., Figure 7). This feature could be used to perform velocity analysis to improve the reference velocity model and the resulting images (e.g., Burdick et al., 2013), a topic which is not addressed here. Additionally, only free-surface phases associated with *P* wave sources have been used to image in this study (Figure 7); however, the proposed method could also be applied to multiples from *S* wave sources (e.g., Wittlinger et al., 2009; Yu et al., 2013). How best to combine the images from the different scattering phases into a single result remains an unresolved issue. Several nonlinear stacking methods have been proposed for this task (Tauzin et al., 2016; Wilson & Aster, 2005) which aims to enhance features that are common between different images. One problem with this approach is that the different phases can be sensitive to different parts of the imaging target and may be removed by stacking. For example, a phase-weighted multimode stack is presented in Figure 11. The stacking effectively down-weights most of the

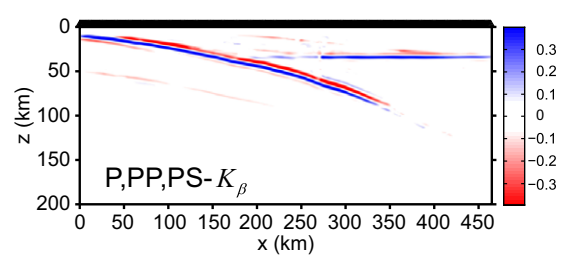


Figure 11. Nonlinear multimode image stacks for the P wave receiver function data set. The phase-weighted stack (Tauzin et al., 2016) of the K_{β} kernel images for the direct arrival (Figure 6a) and the two free-surface phases (Figures 7c and 7d). The constituent images are amplitude normalized prior to stacking.

incorrectly migrated energy of the constituent receiver function images. However, the stacking also removes the vertical boundary of the mantle wedge and the rightmost part of the slab, both of which are only well resolved in the K_{β} image for the direct P wave (Figure 4a). The scattering kernels in equation (10) are derived by applying the adjoint of the forward modeling operator but the imaging method is neither iterative nor is it a formal inversion. The kernel approach could be adapted to perform a migration inversion, potentially reducing imaging artifacts associated with the limited source-receiver geometry and spatial undersampling, as well as allowing for image regularization (e.g., Nemeth et al., 1999; Wilson & Aster, 2005) and simultaneous imaging with multiple phases.

7. Conclusions

A new teleseismic scattered wave imaging method is presented that is suitable for use with both *P* and *S* wave receiver function data in 3-D. The efficacy of the method is demonstrated by imaging the discontinuity structure of a hypothetical subduction zone model using synthetic teleseismic waveforms calculated for a realistic range of illumination angles and a modest number of sources. Examples of the ray theoretical scattering kernels and synthetic imaging results illustrate the complementary characteristics of different scattering modes and the utility of the free-surface phases. The scattering kernels provide a practical and computationally efficient framework for integrative use of *P* and *S* wave receiver functions for imaging in complex structural settings. In subduction zone settings, application of the kernel imaging approach could enable resolution of relatively subtle or steeply dipping interfaces that may not be accurately resolved otherwise.

Acknowledgments

The Matlab implementation of the GRT imaging method was provided by Stephane Rondenay. Two anonymous reviewers provided constructive feedback. The synthetic receiver function data sets and two wavefield animations for the subduction zone model have been included in the supporting information. A Matlab script for calculating the scattering kernels in Figure 2 is also included. This research was supported by NSF-EAR 1318856 and 1554908.

References

- Abers, G. A., MacKenzie, L. S., Rondenay, S., Zhang, Z., Wech, A. G., & Creager, K. C. (2009). Imaging the source region of Cascadia tremor and intermediate-depth earthquakes. *Geology*, 37(12), 1119–1122. https://doi.org/10.1130/G30143A.1
- Abt, D. L., Fischer, K. M., French, S. W., Ford, H. A., Yuan, H., & Romanowicz, B. (2010). North American lithospheric discontinuity structure imaged by Ps and Sp receiver functions. *Journal of Geophysical Research*, 115, B09301, https://doi.org/10.1029/2009JB006914
- Audet, P., Bostock, M. G., Christensen, N. I., & Peacock, S. M. (2009). Seismic evidence for overpressured subducted oceanic crust and megathrust fault sealing. *Nature*, 457(7225), 76–78. https://doi.org/10.1038/nature07650
- Baker, B., & Roecker, S. (2014). A full waveform tomography algorithm for teleseismic body and surface waves in 2.5 dimensions. *Geophysical Journal International*, 198(3), 1775–1794. https://doi.org/10.1093/gjj/ggu236
- Beylkin, G., & Burridge, R. (1990). Linearized inverse scattering problems in acoustics and elasticity. Wave Motion, 12(1), 15–52. https://doi.org/10.1016/0165-2125(90)90017-X
- Bostock, M. G. (2002). Kirchhoff-approximate inversion of teleseismic wavefields. *Geophysical Journal International*, 149, 787–795. https://doi.org/10.1046/j.1365-246X.2002.01687.x
- Bostock, M. G., Hyndman, R. D., Rondenay, S., & Peacock, S. M. (2002). An inverted continental Moho and serpentinization of the forearc mantle. *Nature*, 417(6888), 536–538. https://doi.org/10.1038/417536a
- Bostock, M. G., Rondenay, S., & Shragge, J. (2001). Multiparameter two-dimensional inversion of scattered teleseismic body waves: 1. Theory for oblique incidence. *Journal of Geophysical Research*, 106(B12), 30771–30782. https://doi.org/10.1029/2001JB000330
- Burdick, S., de Hoop, M. V., Wang, S., & van der Hilst, R. D. (2013). Reverse-time migration-based reflection tomography using teleseismic free surface multiples. *Geophysical Journal International*, 196(2), 996–1017. https://doi.org/10.1093/gii/ggt428
- Cerveny, V. (2005). Seismic ray theory. Cambridge, UK: Cambridge University Press.
- Chang, W. F., & McMechan, G. A. (1987). Elastic reverse-time migration. *Geophysics*, 52(10), 1365–1375. https://doi.org/10.1190/1.1442249 Chen, L., Wen, L., & Zheng, T. (2005). A wave equation migration method for receiver function imaging: 1. Theory. *Journal of Geophysical Research*, 110, B11309. https://doi.org/10.1029/2005JB003665
- Chen, P., Jordan, T. H., & Zhao, L. (2007). Full three-dimensional tomography: A comparison between the scattering-integral and adjoint-wavefield methods. *Geophysical Journal International*. 170(1). 175–181. https://doi.org/10.1111/i.1365-246X.2007.03429.x
- Cheng, C., Bodin, T., & Allen, R. M. (2016). Three-dimensional pre-stack depth migration of receiver functions with the fast marching method: A Kirchhoff approach. *Geophysical Journal International*, 205(2), 819–829. https://doi.org/10.1093/gjj/ggw062
- Claerbout, J. F. (1971). Toward a unified theory of reflector mapping. *Geophysics*, 36(3), 467–481. https://doi.org/10.1190/1.1440185 Dahlen, F. A., Hung, S. H., & Nolet, G. (2000). Fréchet kernels for finite-frequency traveltimes: I. Theory. *Geophysical Journal International*, 141(1), 157–174. https://doi.org/10.1046/i.1365-246X.2000.00070.x
- Dueker, K. G., & Sheehan, A. F. (1997). Mantle discontinuity structure from midpoint stacks of converted P to S waves across the Yellow-stone hotspot track. *Journal of Geophysical Research*, 102(B4), 8313–8327. https://doi.org/10.1029/96JB03857
- Duru, K., Kreiss, G., & Mattsson, K. (2014). Stable and high-order accurate boundary treatments for the elastic wave equation on second-order form. SIAM Journal on Scientific Computing, 36(6), A2787–A2818. https://doi.org/10.1137/130947210
- Faber, S., & Müller, G. (1980). Sp phases from the transition zone between the upper and lower mantle. *Bulletin of the Seismological Society of America*, 70(2), 487–508.
- Fichtner, A. (2010). Full seismic waveform modelling and inversion. Berlin, Germany: Springer Science & Business Media.
- Fischer, K. M., Ford, H. A., Abt, D. L., & Rychert, C. A. (2010). The lithosphere-asthenosphere boundary. *Annual Review of Earth and Planetary Sciences*, 38, 551–575. https://doi.org/10.1146/annurev-earth-040809-152438
- Ford, H. A., Fischer, K. M., Abt, D. L., Rychert, C. A., & Elkins-Tanton, L. T. (2010). The lithosphere-asthenosphere boundary and cratonic lithospheric layering beneath Australia from Sp wave imaging. *Earth and Planetary Science Letters*, 300(3), 299–310. https://doi.org/10.1016/j.epsl.2010.10.007
- Gauthier, O., Virieux, J., & Tarantola, A. (1986). Two-dimensional nonlinear inversion of seismic waveforms: Numerical results. *Geophysics*, 51(7), 1387–1403. https://doi.org/10.1190/1.1442188
- Gee, L. S., & Jordan, T. H. (1992). Generalized seismological data functionals. *Geophysical Journal International*, 111(2), 363–390. https://doi.org/10.1111/j.1365-246X.1992.tb00584.x
- Gilbert, H. (2012). Crustal structure and signatures of recent tectonism as influenced by ancient terranes in the western United States. *Geosphere*, 8(1), 141–157. https://doi.org/10.1130/GES00720.1
- Hansen, S. M., & Dueker, K. (2009). P-and S-wave receiver function images of crustal imbrication beneath the Cheyenne Belt in southeast Wyoming. *Bulletin of the Seismological Society of America*, 99(3), 1953–1961. https://doi.org/10.1785/0120080168
- Hansen, S. M., Dueker, K., & Schmandt, B. (2015). Thermal classification of lithospheric discontinuities beneath USArray. *Earth and Planetary Science Letters*, 431, 36–47. https://doi.org/10.1016/j.epsl.2015.09.009
- Herrmann, R. B. (2013). Computer programs in seismology: An evolving tool for instruction and research. Seismological Research Letters, 84, 1081–1088. https://doi.org/10.1785/0220110096

- Hopper, E., Ford, H. A., Fischer, K. M., Lekic, V., & Fouch, M. J. (2014). The lithosphere—asthenosphere boundary and the tectonic and magmatic history of the northwestern United States. Earth and Planetary Science Letters, 402, 69–81.
- Hopper, E., Fischer, K. M., Wagner, L. S., & Hawman, R. B. (2017). Reconstructing the end of the Appalachian orogeny. *Geology*, 45(1), 15–18. https://doi.org/10.1130/G38453.1
- Jordan, T. H., & Frazer, L. N. (1975). Crustal and upper mantle structure from Sp phases. *Journal of Geophysical Research*, 80(11), 1504–1518. https://doi.org/10.1029/JB080i011p01504
- Kennett, B. L. N., Engdahl, E. R., & Buland, R. (1995). Constraints on seismic velocities in the Earth from traveltimes. *Geophysical Journal International*, 122(1), 108–124. https://doi.org/10.1111/j.1365-246X.1995.tb03540.x
- Kind, R., Yuan, X., & Kumar, P. (2012). Seismic receiver functions and the lithosphere-asthenosphere boundary. *Tectonophysics*, 536, 25–43. https://doi.org/10.1016/j.tecto.2012.03.005
- Komatitsch, D., & Tromp, J. (1999). Introduction to the spectral element method for three-dimensional seismic wave propagation. *Geophysical Journal International*, 139(3), 806–822. https://doi.org/10.1046/j.1365-246x.1999.00967.x
- Kumar, P., Yuan, X., Kind, R., & Kosarev, G. (2005). The lithosphere-asthenosphere boundary in the Tien Shan-Karakoram region from S receiver functions: Evidence for continental subduction. *Geophysical Research Letters*, 32, L07305. https://doi.org/10.1029/
- Langston, C. A. (1979). Structure under Mount Rainier, Washington, inferred from teleseismic body waves. *Journal of Geophysical Research*, 84(B9), 4749–4762. https://doi.org/10.1029/JB084iB09p04749
- Lawrence, J. F., & Shearer, P. M. (2006). A global study of transition zone thickness using receiver functions. *Journal of Geophysical Research*, 111, B06307. https://doi.org/10.1029/2005JB003973
- Lekić, V., & Fischer, K. M. (2014). Contrasting lithospheric signatures across the western United States revealed by Sp receiver functions. Earth and Planetary Science Letters, 402, 90–98. https://doi.org/10.1016/j.epsl.2013.11.026
- Lekić, V., & Fischer, K. M. (2017). Interpreting spatially stacked Sp receiver functions. Geophysical Journal International, 210(2), 874–886. https://doi.org/10.1093/gjji/ggx206
- Lekic, V., French, S. W., & Fischer, K. M. (2011). Lithospheric thinning beneath rifted regions of Southern California. *Science*, 334(6057), 783–787. https://doi.org/10.1126/science.1208898
- Levander, A., & Miller, M. S. (2012). Evolutionary aspects of lithosphere discontinuity structure in the western US. *Geochemistry, Geophysics, Geosystems*, 13, Q0AK07. https://doi.org/10.1029/2012GC004056
- Levander, A., Niu, F., & Symes, W. W. (2005). Imaging teleseismic P to S scattered waves using the Kirchhoff integral. In A. Levander & G. Nolet (Eds.), Array analysis of broadband seismograms (pp. 149–170). Washington, DC: American Geophysical Union.
- Liu, K., & Levander, A. (2012). Three-dimensional Kirchhoff-approximate generalized Radon transform imaging using teleseismic P-to-S scattered waves. *Geophysical Journal International*, 192(3), 1196–1216. https://doi.org/10.1093/gji/ggs073
- Mattsson, K. (2012). Summation by parts operators for finite difference approximations of second-derivatives with variable coefficients. Journal of Scientific Computing, 51(3), 650–682. https://doi.org/10.1007/s10915-011-9525-z
- McCrory, P. A., Blair, J. L., Waldhauser, F., & Oppenheimer, D. H. (2012). Juan de Fuca slab geometry and its relation to Wadati-Benioff zone seismicity. *Journal of Geophysical Research*, 117, B09306. https://doi.org/10.1029/2012JB009407
- Monteiller, V., Chevrot, S., Komatitsch, D., & Fuji, N. (2013). A hybrid method to compute short-period synthetic seismograms of teleseismic body waves in a 3-D regional model. *Geophysical Journal International*, 192(1), 230–247. https://doi.org/10.1093/gji/ggs006
- Monteiller, V., Chevrot, S., Komatitsch, D., & Wang, Y. (2015). Three-dimensional full waveform inversion of short-period teleseismic wavefields based upon the SEM-DSM hybrid method. *Geophysical Journal International*, 202(2), 811–827. https://doi.org/10.1093/gji/ggv189
- Morozov, I. B. (2004). Crustal scattering and some artifacts in receiver function images. Bulletin of the Seismological Society of America, 94(4), 1492–1499. https://doi.org/10.1785/012003117
- Nábělek, J., Hetényi, G., Vergne, J., Sapkota, S., Kafle, B., Jiang, M., ... Huang, B. S. (2009). Underplating in the Himalaya-Tibet collision zone revealed by the Hi-CLIMB experiment. Science, 325(5946), 1371–1374. https://doi.org/10.1126/science.1167719
- Nemeth, T., Wu, C., & Schuster, G. T. (1999). Least-squares migration of incomplete reflection data. *Geophysics*, 64(1), 208–221. https://doi.org/10.1190/1.1444517
- Petersson, N. A., & Sjögreen, B. (2009). An energy absorbing far-field boundary condition for the elastic wave equation. *Communications in Computational Physics*, 6(3), 483–508.
- Plessix, R. E. (2006). A review of the adjoint-state method for computing the gradient of a functional with geophysical applications. *Geophysical Journal International*, 167(2), 495–503. https://doi.org/10.1111/j.1365-246X.2006.02978.x
- Poppeliers, C., & Pavlis, G. L. (2003). Three-dimensional, prestack, plane wave migration of teleseismic P-to-S converted phases: 2. Stacking multiple events. *Journal of Geophysical Research*, 108(B5), 2267. https://doi.org/10.1029/2001JB000216
- Rawlinson, N., & Sambridge, M. (2004). Wave front evolution in strongly heterogeneous layered media using the fast marching method. Geophysical Journal International, 156(3), 631–647. https://doi.org/10.1111/j.1365-246X.2004.02153.x
- Rondenay, S. (2009). Upper mantle imaging with array recordings of converted and scattered teleseismic waves. *Surveys in Geophysics*, 30(4–5), 377–405. https://doi.org/0.1007/s10712-009-9071-5
- Rondenay, S., Abers, G. A., & Van Keken, P. E. (2008). Seismic imaging of subduction zone metamorphism. *Geology*, 36(4), 275–278. https://doi.org/10.1130/G24112A.1
- Rondenay, S., Bostock, M. G., & Shragge, J. (2001). Multiparameter two-dimensional inversion of scattered teleseismic body waves 3. Application to the Cascadia 1993 data set. *Journal of Geophysical Research*, 106(B12), 30795–30807. https://doi.org/10.1029/2000JB000039
- Rychert, C. A., & Shearer, P. M. (2009). A global view of the lithosphere-asthenosphere boundary. *Science*, 324(5926), 495–498. https://doi.org/10.1126/science.1169754
- Schmandt, B., & Clayton, R. W. (2013). Analysis of teleseismic P waves with a 5200-station array in Long Beach, California: Evidence for an abrupt boundary to Inner Borderland rifting. *Journal of Geophysical Research: Solid Earth*, 118, 5320–5338. https://doi.org/10.1002/jgrb. 50370
- Schmandt, B., Dueker, K., Humphreys, E., & Hansen, S. (2012). Hot mantle upwelling across the 660 beneath Yellowstone. Earth and Planetary Science Letters, 331, 224–236. https://doi.org/10.1016/j.epsl.2012.03.025
- Selway, K., Ford, H., & Kelemen, P. (2015). The seismic mid-lithosphere discontinuity. Earth and Planetary Science Letters, 414, 45–57. https://doi.org/10.1016/j.epsl.2014.12.029
- Shang, X., Hoop, M. V., & Hilst, R. D. (2012). Beyond receiver functions: Passive source reverse time migration and inverse scattering of converted waves. *Geophysical Research Letters*, *39*, L15308. https://doi.org/10.1029/2012GL052289
- Shearer, P. M. (1991). Constraints on upper mantle discontinuities from observations of long-period reflected and converted phases. *Journal of Geophysical Research*, 96(B11), 18147–18182. https://doi.org/10.1029/91JB01592

AGU Geochemistry, Geophysics, Geosystems

- Shragge, J., Bostock, M. G., & Rondenay, S. (2001). Multiparameter two-dimensional inversion of scattered teleseismic body waves 2. Numerical examples. Journal of Geophysical Research, 106(B12), 30783-30793.
- Stanciu, A. C., Russo, R. M., Mocanu, V. I., Bremner, P. M., Hongsresawat, S., Torpey, M. E., . . . Hole, J. A. (2016). Crustal structure beneath the Blue Mountains terranes and cratonic North America, eastern Oregon, and Idaho, from teleseismic receiver functions. Journal of Geo physical Research: Solid Earth, 121, 5049-5067. https://doi.org/10.1002/2016JB012989
- Svärd, M., & Nordström, J. (2014). Review of summation-by-parts schemes for initial-boundary-value problems, Journal of Computational Physics, 268, 17-38. https://doi.org/10.1016/j.jcp.2014.02.031
- Tarantola, A. (1984). Inversion of seismic reflection data in the acoustic approximation. Geophysics, 49(8), 1259-1266. https://doi.org/10. 1190/1.1441754
- Tauzin, B., Bodin, T., Debayle, E., Perrillat, J.-P., & Reynard, B. (2016). Multi-mode conversion imaging of the subducted Gorda and Juan de Fuca plates below the North American continent. Earth and Planetary Science Letters, 440, 135-146. https://doi.org/10.1016/j.epsl.2016.
- Tong, P., Chen, C. W., Komatitsch, D., Basini, P., & Liu, Q. (2014). High-resolution seismic array imaging based on an SEM-FK hybrid method. Geophysical Journal International, 197(1), 369–395. https://doi.org/10.1093/gji/ggt508
- Tromp, J., Komattisch, D., & Liu, Q. (2008). Spectral-element and adjoint methods in seismology. Communications in Computational Physics, 3(1), 1-32.
- Tromp, J., Tape, C., & Liu, Q. (2005). Seismic tomography, adjoint methods, time reversal and banana-doughnut kernels. Geophysical Journal International, 160(1), 195-216. https://doi.org/10.1111/j.1365-246X.2004.02453.x
- Vidale, J. E., & Houston, H. (1990). Rapid calculation of seismic amplitudes. Geophysics, 55(11), 1504–1507. https://doi.org/10.1190/1.
- Vinnik, L. P. (1977). Detection of waves converted from P to SV in the mantle. Physics of the Earth and Planetary Interiors, 15(1), 39-45. https://doi.org/10.1016/0031-9201(77)90008-5
- Virieux, J., & Operto, S. (2009). An overview of full-waveform inversion in exploration geophysics. Geophysics, 74(6), WCC1-WCC26. https:// doi.org/10.1190/1.3238367
- Wang, Y., Chevrot, S., Monteiller, V., Komatitsch, D., Mouthereau, F., Manatschal, G., . . . Martin, R. (2016). The deep roots of the western Pyrenees revealed by full waveform inversion of teleseismic P waves. Geology, 44(6), 475-478. https://doi.org/10.1130/G37812.1
- Wilson, D., & Aster, R. (2005). Seismic imaging of the crust and upper mantle using regularized joint receiver functions, frequency-wave number filtering, and multimode Kirchhoff migration. Journal of Geophysical Research, 110, B05305. https://doi.org/10.1029/ 2004JB003430
- Wittlinger, G., Farra, V., Hetényi, G., Vergne, J., & Nábělek, J. (2009). Seismic velocities in Southern Tibet lower crust: A receiver function approach for eclogite detection. Geophysical Journal International, 177(3), 1037-1049. https://doi.org/10.1111/j.1365-246X.2008.04084.x
- Yan, J., & Sava, P. (2008). Isotropic angle-domain elastic reverse-time migration. Geophysics, 73(6), S229–S239. https://doi.org/10.1190/1.
- Yu, C. Q., Chen, W. P., & van der Hilst, R. D. (2013). Removing source-side scattering for virtual deep seismic sounding (VDSS). Geophysical Journal International, 195(3), 1932-1941. https://doi.org/10.1093/gji/ggt359
- Yuan, X., Kind, R., Li, X., & Wang, R. (2006). The S receiver functions: Synthetics and data example. Geophysical Journal International, 165(2), 555-564. https://doi.org/10.1111/j.1365-246X.2006.02885.x
- Zhu, H., Luo, Y., Nissen-Meyer, T., Morency, C., & Tromp, J. (2009). Elastic imaging and time-lapse migration based on adjoint methods. Geophysics, 74(6), WCA167-WCA177. https://doi.org/10.1190/1.3261747